

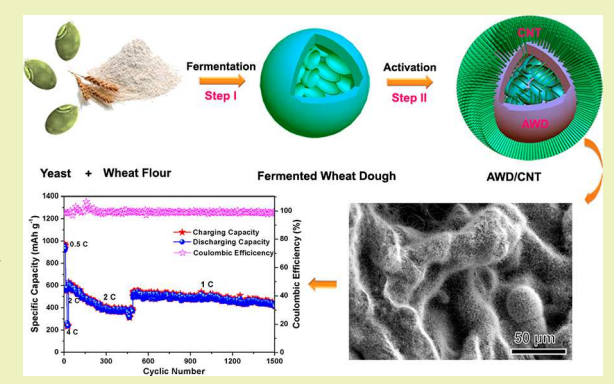
Carbon Nanotubes Derived from Yeast-Fermented Wheat Flour and Their Energy Storage Application

Zan Gao, Ningning Song, Yunya Zhang, Yosyp Schwab, Jiajun He, and Xiaodong Li*

Department of Mechanical and Aerospace Engineering, University of Virginia, 122 Engineer's Way, Charlottesville, Virginia 22904-4746, United States

Supporting Information

ABSTRACT: Worldwide growing commercial interests in applying carbon nanotubes (CNTs) in diverse applications, such as batteries, sensors, catalyst supports, thermal electronics, and high-strength composites, have dramatically expanded the demand for higher CNT production capacity. However, current CNT production is still dominated by relatively high-cost chemical vapor deposition (CVD) methods, which usually involve high temperatures, expensive catalysts, and substantial quantities of nonrenewable petroleum-derived carbon sources. Here, we report that highly dense carbon nanotubes can be derived from yeast-fermented wheat dough scaffolds via a simple, green, and sustainable activation process without using any additional catalysts or extra carbon sources. When the activated wheat dough/carbon nanotube (AWD/ CNT) scaffold is used as a sulfur host to prepare cathode for



lithium-sulfur (Li-S) battery, the assembled Li-S cell exhibited excellent cyclic performance, with a well-retained capacity of ~450 mA h g⁻¹ even after 1500 cycles at a high charge/discharge rate of 1 C. A "self-catalysis" growth mechanism is proposed to explain the formation of the yeast-derived CNTs. Our new findings represent a paradigm shift in developing CNTs and provide a promising solution to obtain advanced renewable carbon materials from natural and abundant biomass materials for use in energy storage applications.

KEYWORDS: Carbon nanotubes, Biomass materials, Yeast, Energy storage, Lithium-sulfur battery

INTRODUCTION

With increasing global energy demand and sobering environmental concerns, efficiently converting and storing energy is paramount.^{1,2} The traditional lithium-ion battery is approaching its theoretical energy density limit and will not be able to satisfy the next-generation needs of larger storage capacity and longer life spans, especially for applications such as electric vehicles (EVs) and off-peak grid energy storage units.^{3,4} Furthermore, the rapidly swelling EV market share is already straining the supply of raw battery materials, and another 3fold production increase of traditional cathode materials is expected by 2020, reaching nearly 400 000 tons per year. Considering their combined detrimental effects of toxicity, nonrenewable nature, and a limited supply of raw materials used in current battery technologies, material sustainability is another critical consideration. Therefore, a different battery chemistry and new material sourcing and fabrication methods are urgently required for sustainable development.

The lithium-sulfur (Li-S) battery has been regarded as the most promising candidate for next-generation high-energy batteries due to its ultrahigh theoretical capacity (1675 mA h g⁻¹), superior specific energy density (~2654 W h kg⁻¹), and the natural abundance of sulfur.^{8–10} However, the successful commercialization of the Li-S battery still faces a plethora of

technical challenges, such as severe capacity degradation, incomplete sulfur utilization, poor cycling life span, bad Coulombic efficiency, which can be ascribed to the insulating nature of sulfur $(\sim 5 \times 10^{-30} \text{ S cm}^{-1} \text{ at } 25 \text{ }^{\circ}\text{C})^{11}$ and the solid reduction products (Li₂S and Li₂S₂), the severe "shuttle effect" of dissolvable intermediates (lithium polysulfides), as well as the uncontrolled lithium-sulfur interface. 12 In the past decade, various approaches, including hybridizing sulfur with different host materials (such as porous carbon, 13-16 graphene oxide, 17-19 carbon nanotubes (CNTs), 20 and conductive polymers^{21,22}), optimizing cell configuration, ^{23,24} designing nanostructured cathodes, 25,26 and adjusting electrolyte composition (by introducing LiNO₃ additives), ²⁷ have all been widely explored to address the aforementioned issues. In particular, hybridizing sulfur with nanostructured carbon hosts is the most promising strategy for efficient electron delivery and effective polysulfide trapping.²⁸

Carbon nanotubes have aroused tremendous interests since the early 1990s, due to their fascinating electronic, magnetic, and mechanical properties, which have been exploited in

Received: March 21, 2018 Revised: June 28, 2018 Published: July 17, 2018



diverse applications, such as batteries, solar cells, sensors, catalyst supports, thermal electronics, and high-strength and magnetic interference shielding composites. 29-38 Specifically, CNTs have been widely used to improve the performances of energy storage devices due to their outstanding electronic and mechanical properties.³⁹ Recently, CNTs have been explored as sulfur hosts because of their extremely large aspect ratio, excellent electrical conductivity, and tubular microstructures, which can be exploited to construct conductive networks and prevent the dissolution of polysulfides.⁴⁰ However, CNTs are typically produced by arc discharge,⁴¹ laser ablation,⁴² or chemical vapor deposition (CVD) methods,^{43,44} all of which involve cumbersome gas handling systems, high-temperature furnaces, consumable catalysts, and complicated postpurification systems, thereby raising the overall production costs. The challenge is, therefore, straightforward: can we engineer largescale CNTs at a low cost and in a sustainable fashion?

Nature renders unlimited and incredible inspiration, which often provides us with hints to overcome difficult challenges such as obtaining battery materials from readily available living organisms.² Biomass materials hold a huge potential to derive advanced carbon materials, including hierarchical activated carbon materials with meso-/micro-pore-size distribution for both supercapacitor and battery applications.⁴⁵ For instance, various biomass materials such as wood and plant tissues, 46,47 agricultural waste, ⁴⁸ activated sludge, ⁴⁹ saw dust, ⁵⁰ and even organic municipal waste ^{51,52} have been successfully applied as precursor materials to produce porous carbon scaffolds, due to their abundant availability, low cost, and competitive performance in a plethora of diverse fields. In our previous studies, cotton textiles, banana peels, and recycled paper have been explored for supercapacitors, lithium-ion batteries, and lithium—sulfur batteries that exhibited exceptional electro-chemical performance. 53-57 As one of the oldest and most important cereal crops, wheat flour has been used for thousands of years and continues to be a staple of the human diet.⁵⁸ Since the natural metabolic process of yeast can leaven the dough and create pores, is it possible to use such leavened dough to obtain nanostructured carbon materials, including CNTs, that can be used as a sulfur host for Li-S battery applications? After all, wheat flour is an abundant, renewable, and inexhaustible natural resource.

In this work, we have successfully derived highly dense CNTs from the yeast-fermented wheat dough scaffolds via a simple, green, and sustainable activation process without relying on any extra catalysts or additional carbon precursors. Highly dense CNTs were found to be vertically grown on the activated dough surface and the interior surfaces of the dough pores. Such an activated wheat dough/CNT (AWD/CNT) scaffold provides a low-cost, scalable, and conductive porous substrate, which can be used as the fundamental building block to host sulfur. As a result, the assembled Li-AWD/CNT/S battery exhibited superior cycling performance with a wellretained capacity of ~450 mA h g⁻¹ even after 1500 cycles at a high charge/discharge rate of 1 C. Here, for the first time, CNTs were derived from renewable yeast-fermented wheat flour without any extra catalysts or additional carbon sources. Unexpectedly, we found that uniform CNT forests/yarns can be fabricated on other substrates, such as the Cu foils and Si wafers simply by activating a thin layer yeast-fermented wheat flour coating. Such a new biomass-derived synthesis method greatly expands the current understanding of CNT fabrication

and suggests a new direction for developing next-generation electronics and energy storage devices from biomass.

EXPERIMENTAL SECTIONS

Preparation of Activated Wheat Dough Coated with Carbon Nanotubes (AWD/CNTs) from the Yeast-Fermented Wheat Dough. Commercially available all-purpose unbleached wheat flour (Pillsbury) and yeast powder (Angel Yeast) were directly purchased and used without further treatment. The carbon nanotubes (CNTs) were formed on both the inner and outer surfaces of porous activated wheat dough (AWD) via a simple one-step heat treatment of yeast-fermented wheat dough. Typically, a cup of wheat flour and some amount of yeast powder were first mixed together via stirring with warm water until the wheat flour was transformed into dough. After that, the wheat dough was kept in the dark at room temperature for 4 h to leaven the dough. When the size of wheat dough doubled, the fermented wheat dough was tipped out and further kneaded into a strong dough with a smooth surface. Then, the fermented wheat dough was further cut into small pieces and put into a crucible, which was further dried under 50 °C for 6 h before activation. After drying, the fermented wheat dough was further expanded around the crucible with inner porous structure. Finally, the crucible together with the yeast-fermented wheat dough was transferred into a horizontal tube furnace, heated to 750 °C, and held for 2 h with a continuous argon gas flow (300 sccm). During the heating process, highly dense CNTs were formed simultaneously on the outer surfaces and inner pore walls of the AWD. After cooling to room temperature, the as-obtained AWD/CNT was washed with distilled water to remove the residual impurities and dried at 80 °C for 6 h. In order to identify the role of yeast in the formation of CNTs, we performed the same activation process of pure wheat dough without fermentation.

Hybridization of AWD/CNT and Sulfur To Prepare AWD/ CNT/S Composite Cathode. The hybridization of activated wheat dough with CNTs and sulfur was carried out in a two-step heat treatment method. First, a certain amount of AWD/CNT was mixed with some amount of sulfur powder, which was then ground and thermally treated at 156 °C for 12 h in a sealed autoclave to infiltrate sulfur into the pores and cavities of the AWD/CNT. After the thermal treatment, sulfur nanoparticles were homogeneously anchored on or penetrated into the inner pores of AWD/CNT to form an AWD/ CNT/S composite. Furthermore, the AWD/CNT/S composite was maintained at 200 °C for 3 h to reduce residual sulfur sticking on the outer surface of the AWD and enable a homogeneous distribution of sulfur within the AWD/CNT. In this work, the mass ratio of AWD/ CNT and S was controlled by 1:2. The sulfur content in the AWD/ CNT/S composite was calculated using thermogravimetric analysis (TGA), with the final AWD/CNT/S exhibiting sulfur content of 65.9 wt % (Figure S1).

Characterization Methods. The microstructure of the prepared samples was characterized by scanning electron microscope (SEM; FEI Quanta 650 with energy-dispersive X-ray spectroscopy (EDS) detector) and transmission electron microscope (TEM; JEOL 2000FX), and high-resolution transmission electron microscopy (HRTEM, FEI Titan). The basic material properties of the synthesized products were determined by X-ray diffraction (XRD; PANalytical X'Pert Pro Multi-Purpose diffractometer (MPD) equipped with Cu K α radiation with $\lambda = 0.15406$ nm), Raman spectroscopy (Renishaw InVia Raman microscope at 514 nm with 5% laser power), X-ray photoelectron spectroscopy (XPS; PHI VersaProbe III, Physical Electronics), and atomic force microscope (AFM; Dimension Icon with ScanAsyst, Bruker). The sulfur content of the composite was performed by thermogravimetric analysis (TGA; Q50,

Characterization of the Mechanical Properties of Individual CNTs. In order to investigate the deformation behavior and measure the elastic modulus of individual CNTs, they were first detached from the substrate and then dispersed into ethanol by ultrasonic treatment. A few drops of such ethanol solution containing CNTs were dispersed onto a silicon wafer and dried at room temperature. An atomic force microscope (AFM, Dimension Icon with ScanAsyst, Bruker) in

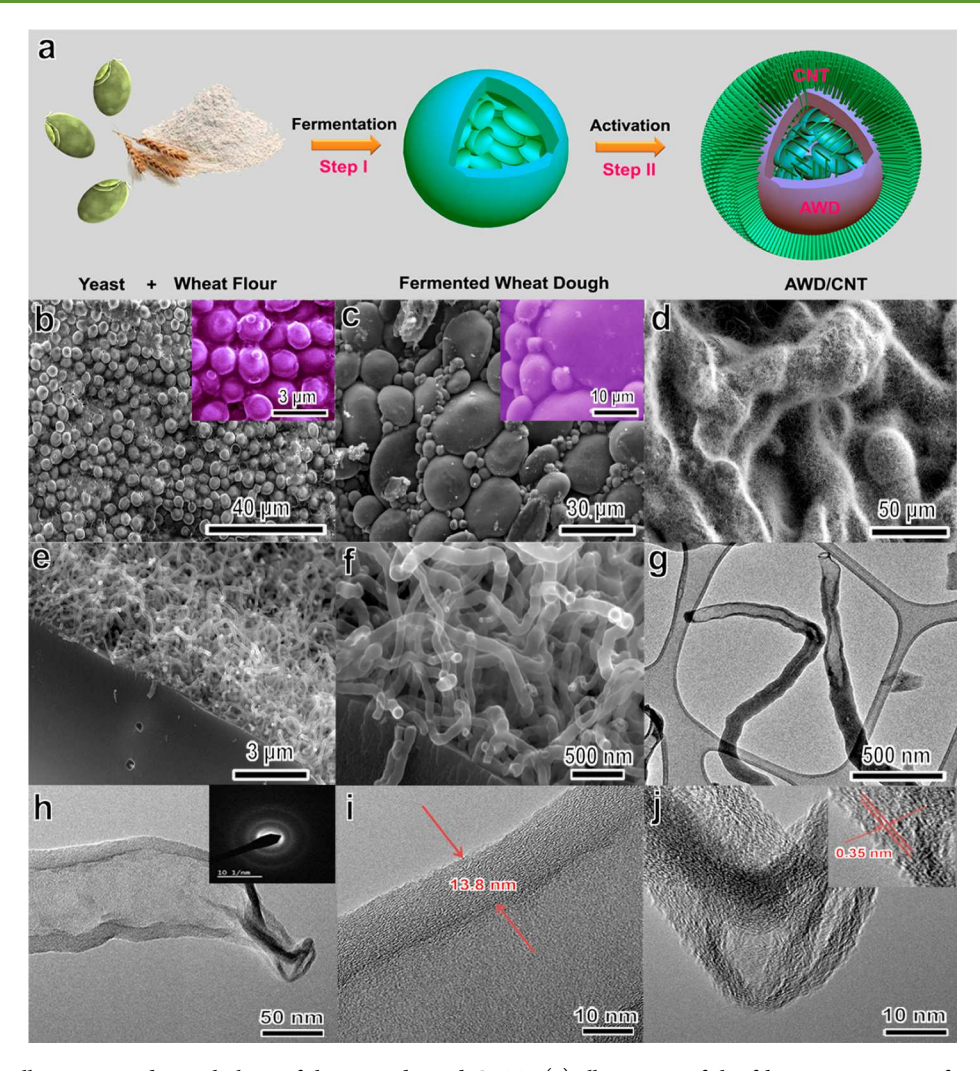


Figure 1. Schematic illustration and morphology of the yeast-derived CNTs. (a) Illustration of the fabrication process of activated wheat dough (AWD) coated with dense carbon nanotubes (CNTs) from the yeast-fermented wheat dough. (b) SEM image of yeast, inset is an amplified region of yeast. (c) SEM image of the yeast-fermented dough, inset is an amplified region. (d) SEM image of the filamentous CNTs on the AWD surface. (e) Cross-sectional SEM images of the filamentous CNTs on the pore walls of AWD. (f) High-magnification SEM images of the filamentous CNTs. (g) TEM image of the individual CNTs. (h) TEM image of the CNT opening tip, inset is the corresponding selected area electron diffraction (SAED) pattern. (i) HRTEM image of the wall of a CNT. (j) HRTEM image of the opening tip of a CNT, inset shows lattice fringes of the tube wall.

tapping mode was applied to locate and image the profile of an individual CNT. For nanoindentation tests, a 40 nm tip radius diamond probe was positioned above the CNT, and several indentations were performed at a constant sampling rate and velocity. The simulation was performed by finite element method (FEM) to further calculate the modulus of the indented CNT.

Electrochemical Characterization of the AWD/CNT/S Composite Cathode. The electrochemical properties of the AWD/ CNT/S composite cathode were measured using CR2032-type coin cells. Briefly, the prepared AWD/CNT/S composite cathode and polyvinyl difluoride (PVDF) with a mass ratio of 90:10 were mixed in N-methylpyrrolidone (NMP) solvent to produce a homogeneous slurry, without using any conductive agent. The resulting mixture was coated onto aluminum foil using a blade to fabricate the working electrode. The prepared AWD/CNT/S cathode was further punched into circular disks and dried at 60 °C for 24 h in a vacuum oven. The sulfur loading on the electrode is ~ 1.5 mg cm⁻².

A lithium-sulfur coin cell was assembled with AWD/CNT/S as a cathode, lithium metal as an anode, and Celgard 2400 film as a separator, respectively. The electrolyte solution with 1 M lithium bis(trifluoromethanesulfonyl)imid (LiTFSI) and 0.2 M LiNO₂ dissolved in 1:1 v/v 1,2-dimethoxyethane (DME) and 1,3-dioxolane

(DOL) solution was used. The CR2032 coin cells were assembled with an MTI MSK-110 crimping machine in an argon-filled glovebox (Mbraun) with oxygen and water contents below 0.1 ppm. The electrolyte-to-sulfur ratio in the assembled cell is ~ 0.133 mL mg⁻¹. Galvanostatic charge/discharge measurements were carried out using a LAND CT2003A battery tester at a voltage window of 1.7 and 2.8 V vs Li/Li⁺. The capacities and charge/discharge rates were calculated based on the mass of active sulfur. A CHI 660E electrochemical workstation was used to measure the cyclic voltammograms and electrochemical impedance spectroscopy (EIS) properties in the frequency range from 0.05 Hz to 100 kHz with an AC perturbation of 5 mV.

RESULTS AND DISCUSSION

Figure 1a schematically illustrates the detailed process of converting yeast-fermented wheat dough into an AWD/CNT scaffold. Typically, natural yeast and wheat flour were mixed together and kneaded into dough, which was then kept at room temperature for 4 h to leaven the dough by the fermentation process of yeast (Step I). After fermentation, the volume of dough is nearly doubled and exhibits a honeycomb-

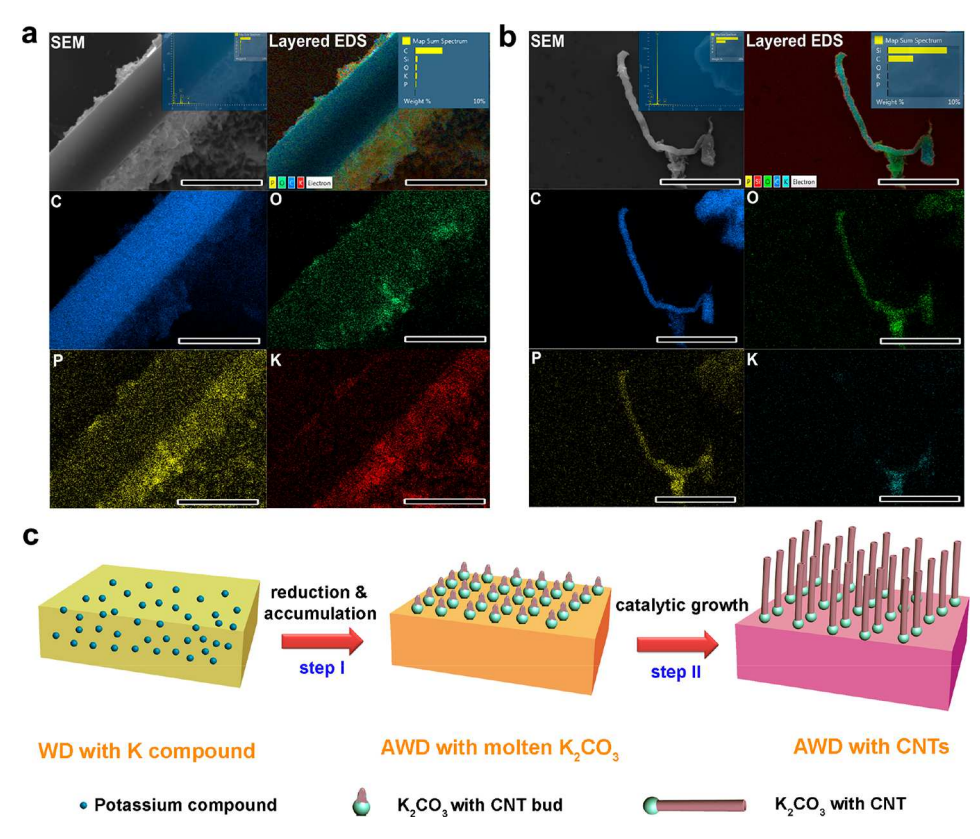


Figure 2. The growth mechanism of the yeast-derived CNTs. (a) SEM image and the corresponding EDS element mapping images of the AWD/ CNT scaffold, inset is the relative element ratio of C, O, P, and K (sample on Si substrate, scale bar 2.5 μ m). (b) SEM image and the corresponding EDS element mapping images of a CNT, inset is the relative element ratio of C, O, P, and K (sample on Si substrate, scale bar 10 µm). (c) Illustration of the proposed "self-catalytic" growth process.

like porous structure due to the metabolic process of yeast. Usually, the fermentation process affects wheat dough via two distinct pathways: On one hand, the growth of yeast cells in the dough self-adheres gluten proteins that form the frames of the inner interconnected networks, which contribute to the extensibility and gas holding capacity of the fermented dough. On the other hand, CO₂ is released during the decomposition of carbohydrates (starch and sugars) via the metastatic reactions of yeast, which is then captured in the dough, leading to the expanded size and interconnected porous structure.⁵⁹ Unexpectedly, after the high-temperature activation process, highly dense CNTs were found to be coated on the activated dough surface and the surface of pore walls of AWD (Step II). This demonstrates that CNTs can be derived from biomass materials without extra catalysts or additional carbon resources throughout the entire reaction process.

Figure S2a shows digital images of the fermented wheat dough before and after activation. SEM imaging (Figure 1b) reveals that yeast cells are oval shaped with diameters ranging from 2 to 5 μ m. Close-up observation shows buds (daughter cells) on the surfaces of parent yeasts (inset of Figure 1b), suggesting the fast-asexual reproduction process of yeast by budding.60 The yeast-fermented dough (Figure 1c) reveals circular disklike starch granules surrounded by spherical yeast cells. The ripples on the surface of the starch granules are imprints of smaller proteins (inset of Figure 1c), which aid in constructing the dough networks and improve elasticity and gas holding properties. Highly dense CNTs were found on the activated dough surface and pore walls of AWD (Figure 1d and Figure S2b). The cross-sectional SEM image of the AWD also

shows that CNTs grew on the pore walls (Figure 1e and Figure S2c). Close-up inspection (Figure 1f and Figure S2d) reveals that CNTs are interwoven amorphously and are 3-20 μ m in length. TEM inspection (Figure 1g) reveals that the CNTs possess a curved filamentous tubular structure with diameters ranging from 100 to 200 nm. Intriguingly, the CNTs have opening tips (Figure 1h). Electron diffraction inspection (inset of Figure 1h) indicates that the phase of the CNTs is hybrid polycrystalline and amorphous. Close-up HRTEM observation unveils that the tube wall has a disordered crystalline structure with variable wall thickness \sim 13.8 nm at the root and \sim 4 nm at the tip (Figure 1i,j). The crystal lattice fringe spacing of the CNTs is ~ 0.35 nm (inset of Figure 1j).

Further studies indicate that, without yeast fermentation, CNTs would not form on the AWD although the AWD still possessed a porous structure (Figure S3). Undoubtedly, yeast fermentation plays a critical role in the formation of CNTs. Therefore, an in-depth understanding of the CNT formation mechanism is required. However, a literature review of current methods of CNT synthesis from renewable biomass, especially without extra catalysts and carbon sources, yields scant results. Here, a series of tests were performed at different growth stages of CNTs to identify the possible growth mechanism (Figures S4-S6). It can be seen that, before activation, both wheat flour and yeast possess a relatively high percentage of elemental C, O, and N, but low P and K (Figures S4 and S5). Interestingly, K and P tend to accumulate on the surface of AWD during the activation process. Specifically, during the initial stage, tadpole-like carbon nanostructures formed on the surface of AWD with smaller buds extruding from carbon

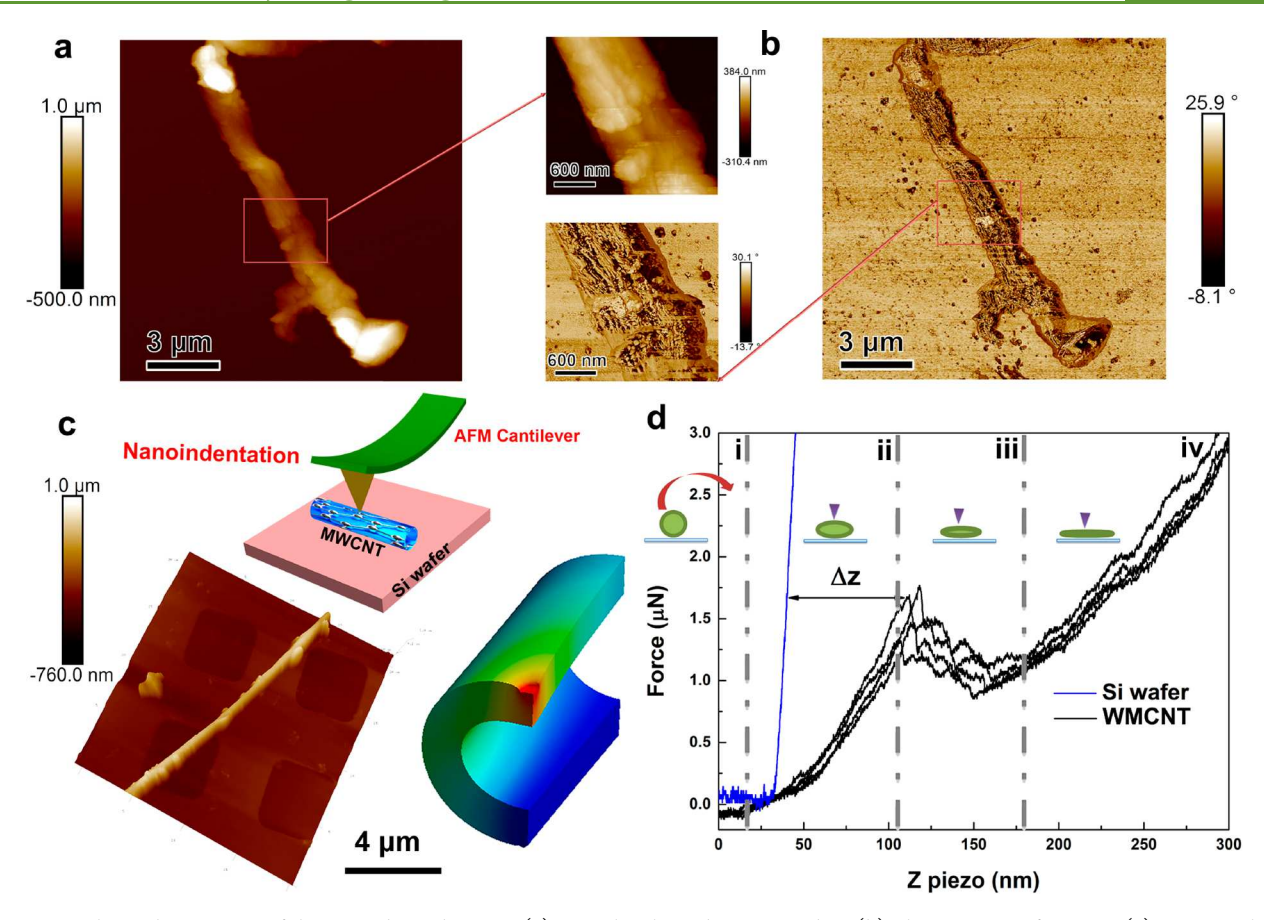


Figure 3. Mechanical properties of the yeast-derived CNTs. (a) AFM height and corresponding (b) phase images of a CNT. (c) AFM 3D height image of a CNT on a Si wafer, a sketch of the adopted nanoindentation setup, and the corresponding finite element simulation results. (d) Cantilever deflection as a function of vertical displacement of Z-piezo, the inset cartoons show the cross-sectional view during the indentation process. Indentation depth Δz is the difference between the Si wafer and a loading curve of a CNT.

spheres (Figure S6). K and P were found to accumulate preferentially on the carbon spheres.

Figure 2a shows the SEM and EDS mapping images of the cross-section of the AWD after the activation process, demonstrating the nature of the K and P concentrations on the surface of pore walls. More interestingly, C, O, and P are all homogeneously distributed along the entire CNT, while elemental K is centered at the root of the tube (Figure 2b). Obviously, the concentration of K is a critical factor in the catalytic growth of CNTs. However, there is a lack of reports associating the catalytic capability of K for the growth of CNTs. Therefore, here we propose a two-step "self-catalysis" process to explain the formation of CNTs (Figure 2c). In the initial fermentation process, CO2 was generated and dissolved into the fermented wet wheat dough by the metabolism of yeast. The dissolved CO2 then reacted with H2O to form carbonic acid; thus K2CO3 and KHCO3 would be the basic forms of potassium compounds. In the following activation step, with the temperature ramped up to 750 °C, potassium compound (mainly K2CO3) will be formed, melted and accumulated on the surface of the activated wheat dough, which can be expressed by the following equation:⁶

$$2KHCO_3 \rightarrow K_2CO_3 + CO_2 + H_2O \tag{1}$$

The molten potassium carbonate could first penetrate the carbon matrix and gradually evaporate and accumulate on the surface of the activated wheat dough. The accumulated potassium carbonate on the surface of the AWD served as

catalysts that initiated the growth of carbon nanotubes via a vapor-liquid-solid (VLS) model. In the VLS model, carbon atoms are supplied to the inner walls by diffusion through the catalyst particle, and the diameter of the CNT is determined by the size of the catalyst. 62 As activation continued, the diameter of the K2CO3 catalyst particle increased, signified experimentally by the increased root diameter of the CNT, indicating a root-growth mechanism. The formation of CNT was triggered by the self-formed catalyst and was further extruded from the carbon spheres by the diffusion of carbon atoms from the bulk catalyst. The formed molten potassium carbonate particle was unstable and continuously varied in size, leading to the curved morphology and tapering of the CNTs. The metastasis and fermentation of yeast lead to the decomposition of long-chain carbohydrates (such as starch and complex sugars) into shortchain carbohydrates (fructose, maltose, glucose, etc.), alcohol and lactic acid, which could be more easily decomposed to hydrocarbons (CH₄), carbon monoxide, hydrogen, and H₂O during the temperature ramp-up stage. On the other hand, the fermentation process also resulted in gluten proteins sticking together that contributed to the increased extensibility and gas holding properties of the fermented dough. The held CO2 gas not only helped lift the dough but also was a key factor in the formation of pores inside the dough. Finally, such unique porous structures aided in the decomposition of the trapped hydrocarbon gas and facilitated the diffusion of carbon atoms through the formed catalyst, providing an ideal environment for the growth of CNTs. The possible self-catalysis growth

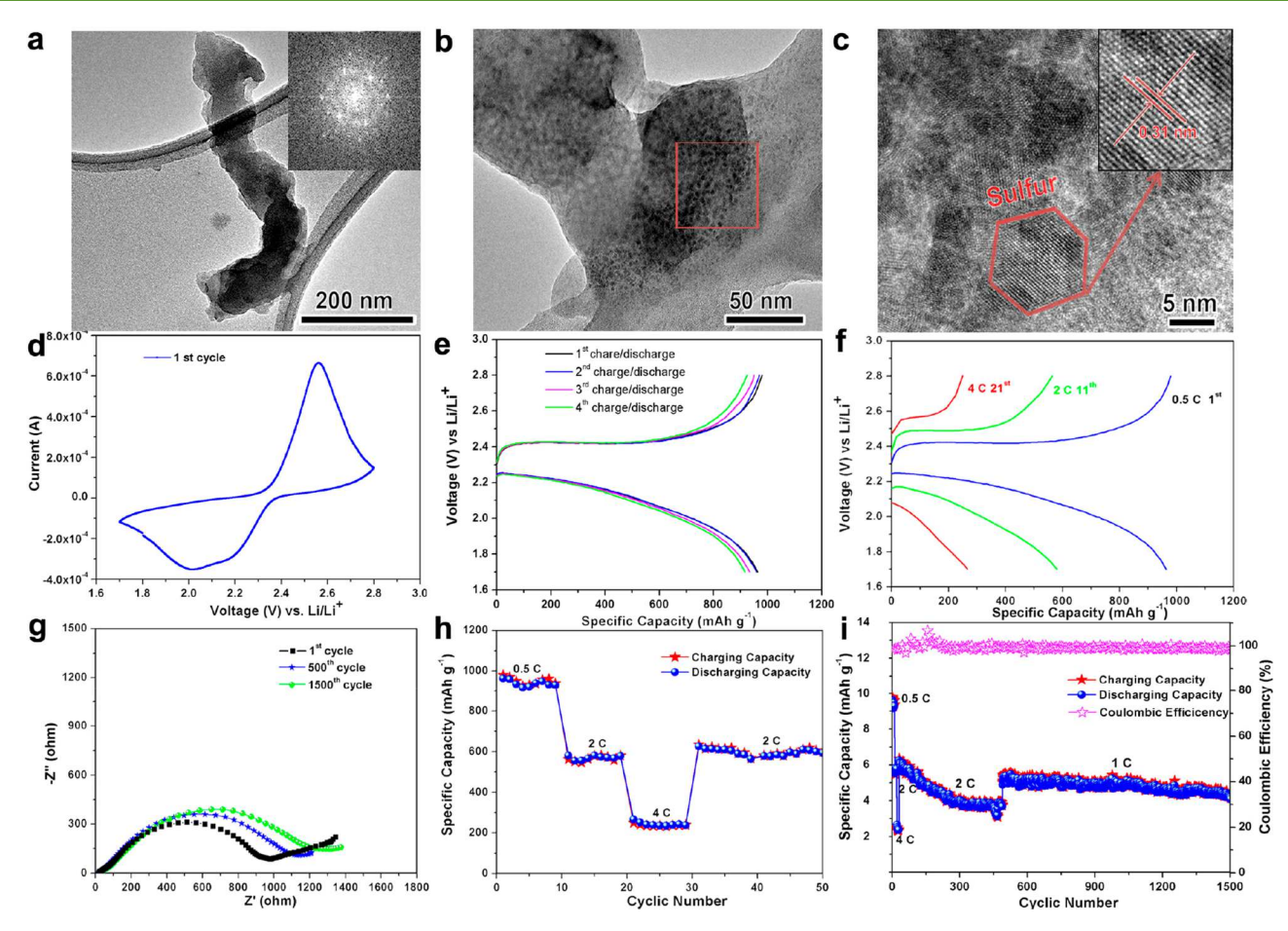


Figure 4. Electrochemical properties of the yeast-derived CNT lithium—sulfur batteries. (a) TEM image of a CNT/S (the CNT filled with sulfur nanoparticles), inset is the corresponding FFT pattern. (b) HRTEM image of the CNT/S. (c) Close-up of the CNT/S, inset is an amplified HRTEM image showing the lattice fringe of sulfur. (d) Cyclic voltammogram (CV) profiles of the AWD/CNT/S electrode at the first cyclic test (scan rate 0.1 mV s⁻¹). (e) First few charge/discharge curves of the assembled Li-AWD/CNT/S battery at a current density of 0.5 C (1 C = 0.24 mA cm⁻²). (f) 1st, 11th, and 21st charge/discharge curves of the AWD/CNT/S electrode at the different charge/discharge rates. (g) Nyquist plots of the AWD/CNT/S electrode at 1st, 500th, and 1500th cycles. (h) Rate performance of the AWD/CNT/S electrode during the first 50 cycles at different charge/discharge rates. (i) Cyclic performance and corresponding Coulombic efficiency of the AWD/CNT/S electrode for the first 1500 cycles.

processes of the CNT from yeast-fermented wheat flour can be summarized as follows: (1) The fermentation process of yeast leads to the decomposition of long-chain carbohydrates to short-chain carbohydrates, which will be further decomposed to CH_4 , H_2 , CO, and H_2O during the high-temperature activation process. (2) The inner potassium compounds in the fermented wheat flour are decomposed to K_2CO_3 , which will melt, evaporate, and accumulate on the surface of activated wheat flour to provide nucleation sites for the clustering of carbon atoms. (3) The nucleated carbon atoms first dissolve into the molten K_2CO_3 nanoparticles and gradually reassemble to form CNT through the VLS growth model. 63

Based on our proposed "self-catalysis" growth mechanism, we coated different substrates with a thin layer yeast-fermented film and performed the same activation process, with the purpose of constructing CNT forests/yarns on the substrate. As shown in Figure S7, a dense CNT film was successfully fabricated on the Cu and Si substrates, which may provide a simple strategy for fabricating CNT-based electronics.

The CNTs are expected to accommodate the mechanical swelling of sulfur during cycling when used as the sulfur host for Li—S battery. Thus, it is essential to experimentally measure the elastic modulus of the synthesized CNTs. Here, an atomic

force microscope (AFM) tip was used to indent individual CNTs in order to measure their elastic modulus. Figure 3a,b shows the height and the corresponding phase images of a single CNT. The amplified region clearly demonstrates that the CNT surface is rough with small patches (insets between Figure 3a and Figure 3b). The AFM 3D height image of a CNT on a Si wafer (Figure 3c) and the corresponding sketch of the nanoindentation setup (inset of Figure 3c) allowed for mechanical property calculations. Force-displacement curves were recorded from an array of indentations on the CNT, and each curve can be separated into four distinct stages (Figure 3d). In stage I, the AFM probe was positioned over the CNT and lowered without causing deformation to the nanotube. In stage II, contact force was linearly increased to a critical value, \sim 1.5 μ N. While continuously pressed, the force was decreased (signified by a nonlinear response) in stage III, which could be ascribed to the hollow shell geometry of the CNT. In this stage, the CNT with a shell-like structure underwent bending deformation. As the inner cavity was further squeezed in stage IV, the indentation force curve followed an elastic linear behavior, because the compressed CNT responded as a homogeneous solid material in this state. These unique features of the indentation force-displacement curves further confirm the hollow cylindrical shell structure of the CNTs. 64,65 The simulated contour of a deformed CNT was calculated using a finite element method (FEM) (inset of Figure 3c). By fitting the slope of $F-\Delta z$ curve in stage I, the elastic modulus of the CNT was determined to be 7.2 ± 0.1 GPa, which is lower than that of single walled or multiwalled CNTs obtained by traditional chemical synthesis methods. The surface modulus and adhesion profiles of a single CNT (Figure S8) exhibited an average surface modulus of \sim 8.52 GPa. The lower elastic modulus of CNTs indicates that the CNTs can deform easily in the elastic regime and consequently help accommodate the volume change of sulfur during the battery charge/discharge cycle.

To demonstrate the energy storage application of AWD/ CNT in Li-S battery, an AWD/CNT/S electrode was fabricated by loading sulfur powder onto the AWD/CNT scaffold via a two-step heat treatment to infiltrate sulfur into the pores of the AWD and the inner tubes of the CNTs. SEM inspection (Figure S9a-c) shows that CNTs infiltrated with sulfur lay on the surface of AWD due to the strong interaction between the sulfur-impregnated CNTs and the AWD substrate. The comparison of the TEM images of pure AWD/CNT and AWD/CNT/S showed that a multitude of nanoparticles was deposited on the surface of amorphous carbon substrate (Figure S10, Figure 4a). HRTEM (Figure 4b,c) observations further confirm that these nanoparticles are sulfur with diameters ranging from 3 to 5 nm. 66 CNTs with open tips not only served conductors for fast electron and ion transport, but also accommodated the large volume change of sulfur during the electrochemical reaction process. The sulfur nanoparticles exhibit a lattice fringe spacing of ~0.31 nm (inset of Figure 4c), which can be indexed to the (313) crystal plane of the orthorhombic structure of sulfur (JCPDS 24-0733). Raman spectrum (Figure S9d) and X-ray diffraction (XRD) (Figure S9e) were further used to validate the reaction between sulfur and AWD/CNT.

Figure S9d shows the XRD patterns of yeast, pure wheat flour, AWD/CNT, and AWD/CNT/S composites. The broad diffraction peak at about $2\theta = 20^{\circ}$ for the yeast corresponds to the amorphous structure of yeast cells. The diffraction peaks of wheat flour between 5° and 35° suggest the typical A-type diffraction pattern of cereal starches. After activation, the characteristic peaks of wheat flour disappear; instead, two broader diffraction peaks around 25° and 45° present in the XRD spectrum, pointing toward the (002) and (100) characteristic peaks of amorphous multiwalled carbon nanotubes. 69 The feature peaks of CNTs disappeared in the XRD patterns of AWD/CNT/S composite, which demonstrated the standard diffraction peaks of the orthorhombic structure sulfur (JCPDS 24-0733), agreeing well with the HRTEM results. Raman spectroscopy was further used to validate the reaction between sulfur and CNTs (Figure S9e), which is often used to characterize the ordered/disordered structure of graphitic materials.⁷⁰ In general, the D band at 1350 cm⁻¹ is the breathing mode of point photons of A_{1g} symmetry, resulting from the defects and disordered graphite structures, while the G band at ~1585 cm⁻¹ and 2D band at ~2800 cm⁻¹ are attributed to the first-order scattering of the E_{2g} phonon mode of in-plane sp² C atoms and second-order Raman scattering process, respectively.⁷¹ Compared with the CNTs, the new peaks between 100 and 400 cm⁻¹ in the Raman spectrum of AWD/CNT/S composite can be ascribed to the vibrational modes of sulfur, suggesting the appearance of sulfur in the

composite. The intensity ratio of the D and G bands is a signature of the degree of functionalization of CNTs. The calculated $I_{\rm D}/I_{\rm G}$ ratio (\sim 0.68) of the AWD/CNT/S composite is higher than that of just AWD/CNT alone (0.87), indicating the smaller defects and disordered structures of AWD/CNT/S, which could be attributed to the reaction between sulfur and CNTs, making sulfur penetration into the defects and cavities of CNTs.

X-ray photoelectron spectroscopy (XPS) of the AWD/ CNT/S composite (Figure S11) was used to observe and understand the interaction between sulfur and AWD/CNTs. The survey XPS spectrum of the AWD/CNT/S composite confirmed the presence of sulfur in 3D AWD/CNTs scaffold (Figure S11a). In the C 1s XPS spectrum of AWD/CNT/S composite (Figure S11b), the major peak at 284.8 eV corresponds to the sp² hybridized C-C/C=C, while the peaks at 286.4 and 289.2 eV can be ascribed to C—O and O— C=O, respectively. The peak at 285.5 eV could be ascribed to the presence of C-S, which confirms the reaction between the AWD/CNT substrate and S.66 In the S 2p spectrum (Figure S11c), there is an S $2p_{3/2}$ and $2p_{1/2}$ doublet with an energy separation of 1.2 eV. Compared with the binding energy of pure elemental sulfur (164.0 eV), the relatively lower binding energy of S $2p_{3/2}$ (163.7 eV) further confirms the presence of C—S bonds. The smaller peak at 168.5 eV can be attributed to the formation of sulfate species during the heating process.11

The electrochemical performance of the as-assembled AWD/CNT/S cells was investigated by cyclic voltammetry (CV), galvanostatic charge/discharge tests, and electrochemical impedance spectroscopy (EIS). The traditional CV profile of Li-S batteries usually exhibits two pairs of redox peaks, one pair at \sim 2.3 and \sim 2.0 V, and another pair at \sim 2.35 and ~2.45 V, suggesting a two-stage electrochemical reduction and oxidation of S during the charge/discharge process.⁷ Typically, the first reduction peak at ~2.3 V corresponds to a solid-to-liquid phase transition (from S to Li_2S_n , $n \geq 4$), and the second reduction peak at ~2.0 V involves a liquid-to-solid phase transition (from the dissolved lithium polysulfide to solid Li₂S₂ or LiS₂).⁷⁴ Figure 4d shows the CV curve of the assembled Li-AWD/CNT/S battery at the first cycle, which demonstrates a different single pair of redox peaks, corresponding to the single discharge plateau at ~2.2 V and single charge plateau at \sim 2.5 V (Figure 4e). The first discharge curve shows a sloping, with an initial discharge capacity of \sim 979 mA h g⁻¹, both of which are common characteristics of conversion-type cathode materials (Figure 4e).⁷⁵ The reversible capacities of AWD/CNT/S electrode at the second, third, and fourth cycles are ~ 969 , ~ 950 , and 925 mA h g⁻¹, respectively (Figure 4e). The voltage hysteresis can be attributed to the slow reaction kinetics, while the capacity decay could be ascribed to the decomposition of the electrolyte, the formation of a solid electrolyte interphase (SEI) film, and the dissolution of polysulfides.⁷⁶ The single reduction peak and the accompanying sloping discharge plateau have been regarded as an identifying characteristic of a Li-S battery with lower capacity but better cycle life, suggesting a solid-to-solid phase transition (from the smaller sulfur particle or sulfur-carbon compound to LiS₂) during the electrochemical reaction process. 77,75

Figure 4f shows the representative charge/discharge profiles of the AWD/CNT/S electrode at different charge/discharge rates ranging from 0.5 to 4 C. The reversible capacities at the

Table 1. Comparison of Battery Performance with Various Carbon Materials Used in Lithium-Sulfur Battery Applications

14	MC/CMK- 3^a porous hollow carbon MC-MesoC-TiO $_2$	 1.2 M LiPF₆ solution in ethyl methyl sulphone 1 M LiTFSI in tetra-glyme 1 M LiTFSI in DOL/DME (1:1, v/v) LiNO₃ (0.1 M) 	1320 mA h g ⁻¹ at 168 mA g ⁻¹ 974 mA h g ⁻¹ at 0.5 C	20 100
	MC-MesoC-TiO ₂	87	· ·	100
15	<u>2</u>	1 M LiTESI in DOL/DME (1.1, v/v) LiNO, (0.1 M)	570 A 1 -1 + 0.5 C	
		1 111 E111 01 III E CE, E111E (111) 1, 1, 1 E11 (03 (011 111)	$578 \text{ mA h g}^{-1} \text{ at } 0.5 \text{ C}$	140
16	cores/shell MC/graphene	1 M LiTFSI in DOL/DME (1:1, v/v) LiNO ₃ (0.5 M)	601 mA h g ⁻¹ at 0.5 C	500
17	nitrogen-doped 3D rGO ^b	1 M LiTFSI in DOL/DME (1:1, v/v) LiNO ₃ (0.5 M)	$632 \text{ mA h g}^{-1} \text{ at } 0.5 \text{ C}$	500
19	GO ^c	1 M LiTFSI in PYR14TFSI/PEGDME	$370 \text{ mA h g}^{-1} \text{ at } 2 \text{ C}$	60
20	CNTs	1 M LiTFSI in TEGDME	800 mA h g^{-1} at 200 mA g^{-1}	100
47	microporous char	1 M LiTFSI in DOL/DME (1:1, v/v) LiNO ₃ (0.1 M)	$550 \text{ mA h g}^{-1} \text{ at } 800 \text{ mA g}^{-1}$	150
48	corncob-derived porous carbon	1 M LiTFSI in DOL/DME (1:1, v/v) LiNO ₃ (0.1 M)	554 mA h g ⁻¹ at 0.1 C	50
51	shaddock peel carbon sheets	1 M LiTFSI in DOL/DME (1:1, v/v) LiNO ₃ (0.1 M)	722.5 mA h g ⁻¹ at 0.2 C	100
52	soybean residue-derived NOPC ^d	1 M LiTFSI in DOL/DME (1:1, v/v) LiNO ₃ (0.1 M)	435.7 mA h g ⁻¹ at 1 C	600
our work	yeast-derived AWD/CNT	1 M LiTFSI in DOL/DME (1:1, v/v) LiNO ₃ (0.2 M)	450 mA h g ⁻¹ at 1 C	1500

"MC: microporous carbon. "rGO: reduced graphene oxide. "GO: graphene oxide. "NOPC: nitrogen and oxygen dual-doped porous carbon.

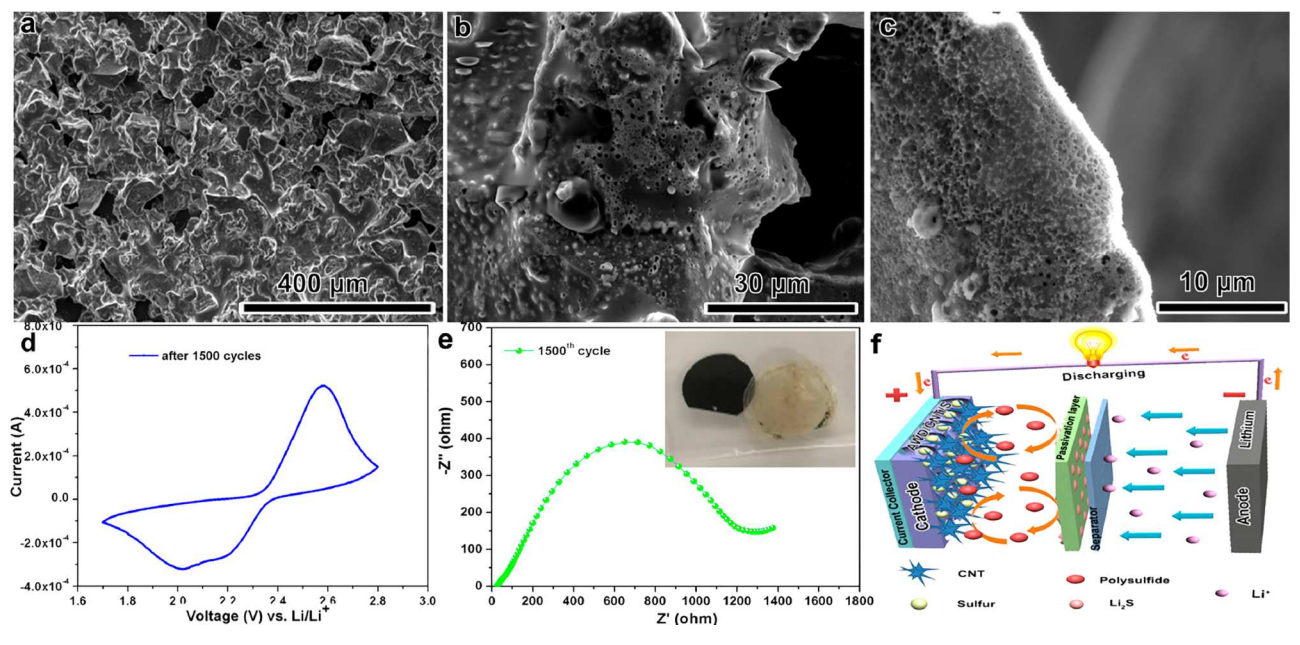


Figure 5. The trapping mechanism of the AWD/CNT/S cathode. (a–c) SEM images of the AWD/CNT/S cathode after 1500 charge/discharge cycles. (d) Cyclic voltammogram profiles of the AWD/CNT/S electrode after 1500 charge/discharge cycles (scan rate 0.1 mV s⁻¹). (e) Nyquist plot of the AWD/CNT/S electrode after 1500 charge/discharge cycles, inset is the digital image of the AWD/CNT/S electrode after 1500 charge/discharge cycles. (f) Schematic illustration of the AWD/CNT/S electrode after 1500 charge/discharge cycles.

first (0.5 C), 11th (2 C), and 31st (4 C) cycles were measured to be ~979, ~562, and ~249 mA h g $^{-1}$, respectively. Figure 4g shows the EIS spectrum of the AWD/CNT/S cell at different cycles. The charge transfer resistance (R_{ct}) can be identified by the diameter of the semicircle arc. ⁷⁹ It can be seen that the R_{ct} of AWD/CNT/S cell increased from \sim 930 Ω (1st cycle) to ~1100 Ω (500th cycle), and finally ~1210 Ω after the 1500th cycle, suggesting eminent stability. Impressively, the AWD/ CNT/S cell exhibited a stable capacity retention during the first 1500 cycles, as demonstrated in Figure 4h,i. Except for the fast decay associated with the initial discharge capacity, the AWD/CNT/S cell remained stable for the first 50 cycles even after increasing the charge/discharge rate from 0.5 to 4 C (Figure 4h). At the charge/discharge rate of 2 C, an obvious capacity decline from \sim 618 mA h g⁻¹ (50th cycle) down to \sim 320 mA h g⁻¹ (500th cycle) was observed. When the charge/ discharge rate was reduced down to 1 C, the capacity was recovered to \sim 540 mA h g⁻¹ (at 501st cycle), which remained stable between 500 and 1500 cycles, with a capacity decay of 0.09 mA h g⁻¹ per cycle (Figure 4i). Except for the initial several cycles, the AWD/CNT/S cell exhibited almost 100% Coulombic efficiency during its entire life span. The battery performance of the AWD/CNT/S cell was compared with previously published various carbon materials in Table 1. Clearly, AWD/CNT/S cathode demonstrated the longest life span. All of these results represented a totally different Li–S chemistry influenced by yeast-derived AWD/CNTs, indicating a significant breakthrough for the development of next-generation high-energy batteries.

In order to fully understand the superior cyclic performance of the AWD/CNT/S electrode, we performed further measurements involving SEM, EDS, CV, and EIS spectrum techniques of the Li–S cell with AWD/CNT/S cathode before and after 1500 cycles (Figure 5, Figures S12 S13). Comparing the AWD/CNT/S cathode before the charging/discharging test (Figure S12a–c), the basic framework of AWD/CNT/S cathode was well-retained even after 1500 cycles (Figure 5a), further demonstrating the outstanding mechanical stability of

AWD/CNT substrate. A thin porous layer was formed on the surface of AWD/CNT after 1500 cycles (Figure 5b,c). The EDS mapping of AWD/CNT/S cathode after 1500 cycles exhibited a more homogeneous S distribution (Figure S13), compared with the EDS mapping of AWD/CNT/S cathode before the charging/discharging test (Figure S12). The unchanged shape and redox peaks of the CV curve after 1500 cycles (Figure 5d) demonstrated robust reversibility of the AWD/CNT/S cell. The increased electron transfer resistance of AWD/CNT/S cathode after 1500 cycles (Figure 5e) could be ascribed to the formation of Li₂S₂/Li₂S passivation layer on the outside surface of AWD/CNT. The porous insulating layer increased the polysulfide trapping capability of the AWD/CNT cathode, as exhibited by the nearly transparent separator film after 1500 cycles (inset of Figure 5e). As illustrated in Figure 5f, a possible trapping mechanism is the formation of a porous, compact nonconductive passivation layer on the outside surface of AWD/ CNT with increased cycles. This porous layer allowed the Li⁺ ions to easily penetrate into the inside of AWD/CNT electrode; meanwhile, the interconnected conductive CNT on inside porous AWD improved the conductivity of AWD/ CNT/S composite. Overall, such a porous passivation layer functioned as an inhibitor, which blocked the dissolution of polysulfides, effectively mitigated the shuttle effect of polysulfides, and finally contributed to the improved life span.

Based on the above results, the exceptional charge/discharge cycling performance of the Li-S battery system, and excellent rate capacity and superior Coulombic efficiency of the asprepared AWD/CNT/S electrode, can be attributed to the following merits: (1) The special composition of yeastfermented wheat dough, consisting of proteins, carbohydrates, lipids, fibers, and minerals,80 renders rich functional groups (such as C-H, -OH, >C=O, -C(=O)OH, and >C= C<) for both the AWD and CNTs. These functional groups further react with sulfur during the high-temperature annealing process, enabling the short-chain sulfur to chemically bond to the surface of the carbon host and form sulfurized C/S compounds, which can significantly reduce the dissolution of lithium polysulfides and improve cycling performance. (2) Highly dense CNTs not only possess rich functional groups but are also doped with elemental N and P, which have strong affinity to sulfur species, significantly reduce the binding energy with lithium polysulfides, and in turn serve as physical barriers for lithium polysulfides. §1 (3) The hollow structure of CNTs not only enabled the penetration of sulfur into the inside of the tubes but also effectively buffered the volume change and protected the structural integrity during the electrochemical reaction process. (4) The CNTs exhibit excellent conductivity, which could further serve as an expressway for electrons, thereby shortening the transportation/diffusion paths for lithium ions and enabling faster kinetics and excellent Coulombic efficiency. (5) A porous passivation layer is formed around the CNT array during the cycling process, which contributed to the blocking of the dissolution of polysulfides and aided in mitigating the shuttle effect of polysulfides. (6) The porous AWD substrate not only increased the specific surface areas but also accommodated the stress induced by the volume change of sulfur, ensuring the structural integrity of the AWD/CNT/S electrode during the charge/discharge process. In general, the individual components of the AWD/CNT/S composite synergistically work together to significantly

mitigate the dissolution of polysulfides, leading to the exceptional electrochemical performance.

CONCLUSION

In summary, honeycomb-like activated wheat dough coated with dense carbon nanotubes (AWD/CNTs) was derived from the yeast-fermented wheat dough. Impressively, highly dense CNTs were found vertically grown on both outside and inside surfaces of AWD. For the first time, CNTs were derived from biomass materials without using any extra catalysts or additional carbon sources. Results demonstrated that yeast was the critical factor in the growth of CNTs from the wheat dough. A "self-catalysis" growth mechanism was proposed to describe the growth of CNTs and expands our current understanding of the catalytic growth of CNTs. All of these results suggest a new possibility and strategy to fabricate nanostructured carbon materials from naturally abundant biomass materials. The basic mechanical properties of a single CNT were investigated using both experimental and simulation methods, which demonstrated an average modulus of ~8.52 GPa. The lower elastic modulus of CNTs was expected to help accommodate the volume change of sulfur during the battery charge/discharge cycle. When used as a sulfur host, the assembled AWD/CNT/S electrode exhibited a superior life span of 1500 cycles. Considering economic and social benefits, such low-cost biomass-based AWD/CNTs composite holds important promises for energy storage applications.

ASSOCIATED CONTENT

S Supporting Information

The Supporting Information is available free of charge on the ACS Publications website at DOI: 10.1021/acssuschemeng.8b01292.

TGA, SEM, EDS mapping, peak force AFM images, XRD, as well as the Raman and XPS spectroscopy of the AWD/CNT and AWD/CNT/S composites (PDF)

AUTHOR INFORMATION

Corresponding Author

*E-mail: xl3p@virginia.edu.

ORCID ®

Zan Gao: 0000-0003-3047-5616 Yunya Zhang: 0000-0002-9411-0184

Notes

The authors declare no competing financial interest.

ACKNOWLEDGMENTS

The U.S. National Science Foundation (CMMI-1728042) provided financial support for this study. The authors thank the staff members at the University of Virginia NMCF for electron microscopy technical support.

■ REFERENCES

- (1) Armand, M.; Tarascon, J.-M. Building better batteries. *Nature* **2008**, *451*, 652–657.
- (2) Bruce, P. G.; Freunberger, S. A.; Hardwick, L. J.; Tarascon, J.-M. Li-O₂ and Li-S batteries with high energy storage. *Nat. Mater.* **2012**, *11*, 19
- (3) Goodenough, J. B. Electrochemical energy storage in a sustainable modern society. *Energy Environ. Sci.* **2014**, 7 (1), 14–18.

- (4) Goodenough, J. B.; Kim, Y. Challenges for rechargeable Li batteries. *Chem. Mater.* **2010**, 22 (3), 587–603.
- (5) Grey, C. P.; Tarascon, J. M. Sustainability and in-situ monitoring in battery development. *Nat. Mater.* **2016**, *16* (1), 45–56.
- (6) Larcher, D.; Tarascon, J.-M. Towards greener and more sustainable batteries for electrical energy storage. *Nat. Chem.* **2015**, 7 (1), 19–29.
- (7) Yan, L.; Wang, H.; Huang, D.; Luo, H. Electrodes with high conductivities for high performance lithium/sodium ion batteries. *Eng. Sci.* **2018**, *1*, 1–50.
- (8) Manthiram, A.; Fu, Y.; Su, Y. S. Challenges and prospects of lithium-sulfur batteries. *Acc. Chem. Res.* **2013**, *46* (5), 1125–1134.
- (9) Seh, Z. W.; Sun, Y.; Zhang, Q.; Cui, Y. Designing high-energy lithium—sulfur batteries. *Chem. Soc. Rev.* **2016**, *45*, 5605–5634.
- (10) Lochala, J.; Liu, D.; Wu, B.; Robinson, C.; Xiao, J. Research progress toward the practical applications of lithium–sulfur batteries. *ACS Appl. Mater. Interfaces* **2017**, *9* (29), 24407–24421.
- (11) Wang, Z.; Dong, Y.; Li, H.; Zhao, Z.; Bin Wu, H.; Hao, C.; Liu, S.; Qiu, J.; Lou, X. W.; David. Enhancing lithium—sulphur battery performance by strongly binding the discharge products on aminofunctionalized reduced graphene oxide. *Nat. Commun.* **2014**, *5*, 5002.
- (12) Evers, S.; Nazar, L. F. New approaches for high energy density lithium—sulfur battery cathodes. *Acc. Chem. Res.* **2013**, 46 (5), 1135—1143.
- (13) Ji, X.; Lee, K. T.; Nazar, L. F. A highly ordered nanostructured carbon-sulphur cathode for lithium-sulphur batteries. *Nat. Mater.* **2009**, *8* (6), 500–506.
- (14) Jayaprakash, N.; Shen, J.; Moganty, S. S.; Corona, A.; Archer, L. A. Porous hollow carbon@sulfur composites for high-power lithium-sulfur batteries. *Angew. Chem., Int. Ed.* **2011**, *50* (26), 5904–5908.
- (15) Zegeye, T. A.; Kuo, C. F. J.; Wotango, A. S.; Pan, C. J.; Chen, H. M.; Haregewoin, A. M.; Cheng, J. H.; Su, W. N.; Hwang, B. J. Hybrid nanostructured microporous carbon-mesoporous carbon doped titanium dioxide/sulfur composite positive electrode materials for rechargeable lithium-sulfur batteries. *J. Power Sources* **2016**, 324, 239–252.
- (16) Zegeye, T. A.; Kuo, C. F. J.; Chen, H. M.; Tripathi, A. M.; Lin, M. H.; Cheng, J. H.; Duma, A. D.; Su, W. N.; Hwang, B. J. Dual-confined sulfur in hybrid nanostructured materials for enhancement of lithium-sulfur battery cathode capacity retention. *ChemElectroChem* **2017**, *4* (3), 636–647.
- (17) Zegeye, T. A.; Tsai, M. C.; Cheng, J. H.; Lin, M. H.; Chen, H. M.; Rick, J.; Su, W. N.; Kuo, C. F. J.; Hwang, B. J. Controllable embedding of sulfur in high surface area nitrogen doped three dimensional reduced graphene oxide by solution drop impregnation method for high performance lithium-sulfur batteries. *J. Power Sources* **2017**, 353, 298–311.
- (18) Wang, H.; Yang, Y.; Liang, Y.; Robinson, J. T.; Li, Y.; Jackson, A.; Cui, Y.; Dai, H. Graphene-wrapped sulfur particles as a rechargeable lithium-sulfur battery cathode material with high capacity and cycling stability. *Nano Lett.* **2011**, *11* (7), 2644–2647.
- (19) Ji, L.; Rao, M.; Zheng, H.; Zhang, L.; Li, Y.; Duan, W.; Guo, J.; Cairns, E. J.; Zhang, Y. Graphene oxide as a sulfur immobilizer in high performance lithium/sulfur cells. *J. Am. Chem. Soc.* **2011**, *133* (46), 18522–18525.
- (20) Guo, J.; Xu, Y.; Wang, C. Sulfur-impregnated disordered carbon nanotubes cathode for lithium-sulfur batteries. *Nano Lett.* **2011**, *11* (10), 4288–4294.
- (21) Zhou, W.; Yu, Y.; Chen, H.; Disalvo, F. J.; Abruña, H. D. Yolkshell structure of polyaniline-coated sulfur for lithium-sulfur batteries. *J. Am. Chem. Soc.* **2013**, *135* (44), 16736–16743.
- (22) Ma, G.; Wen, Z.; Jin, J.; Lu, Y.; Rui, K.; Wu, X.; Wu, M.; Zhang, J. Enhanced performance of lithium-sulfur battery with polypyrrole warped mesoporous carbon/sulfur composite. *J. Power Sources* **2014**, 254, 353–359.
- (23) Su, Y.-S.; Manthiram, A. A new approach to improve cycle performance of rechargeable lithium—sulfur batteries by inserting a free-standing MWCNT interlayer. *Chem. Commun.* **2012**, 48 (70), 8817.

- (24) Gao, Z.; Zhang, Y.; Song, N.; Li, X. Towards flexible lithium-sulfur battery from natural cotton textile. *Electrochim. Acta* **2017**, *246*, 507–516.
- (25) Yang, Y.; Zheng, G.; Cui, Y. Nanostructured sulfur cathodes. *Chem. Soc. Rev.* **2013**, 42 (7), 3018–3032.
- (26) Ma, L.; Hendrickson, K. E.; Wei, S.; Archer, L. A. Nanomaterials: science and applications in the lithium—sulfur battery. *Nano Today* **2015**, *10* (3), 315–338.
- (27) Liang, X.; Wen, Z.; Liu, Y.; Wu, M.; Jin, J.; Zhang, H.; Wu, X. Improved Ccycling performances of lithium sulfur batteries with LiNO₃-modified electrolyte. *J. Power Sources* **2011**, *196* (22), 9839–9843.
- (28) Li, Z.; Huang, Y.; Yuan, L.; Hao, Z.; Huang, Y. Status and prospects in sulfur-carbon composites as cathode materials for rechargeable lithium-sulfur batteries. *Carbon* **2015**, *92*, 41–63.
- (29) Iijima, S. Helical microtubules of graphitic carbon. *Nature* **1991**, 354 (6348), 56–58.
- (30) De Volder, M. F. L.; Tawfick, S. H.; Baughman, R. H.; Hart, A. J. Carbon nanotubes: present and future commercial applications. *Science* **2013**, 339 (6119), 535–539.
- (31) Lin, C.; Hu, L.; Cheng, C.; Sun, K.; Guo, X.; Shao, Q.; Li, J.; Wang, N.; Guo, Z. Nano-TiNb₂O₇/carbon nanotubes composite anode for enhanced lithium-ion storage. *Electrochim. Acta* **2018**, *260*, 65–72.
- (32) Luo, Q.; Ma, H.; Hao, F.; Hou, Q.; Ren, J.; Wu, L.; Yao, Z.; Zhou, Y.; Wang, N.; Jiang, K.; Lin, H.; Guo, Z. Carbon nanotube based inverted flexible perovskite solar cells with all-inorganic charge contacts. *Adv. Funct. Mater.* **2017**, *27* (42), 1703068-1–1703068-8.
- (33) Li, Y.; Zhou, B.; Zheng, G.; Liu, X.; Li, T.; Yan, C.; Cheng, C.; Dai, K.; Liu, C.; Shen, C.; Guo, Z. Continuously prepared highly conductive and stretchable SWNT/MWNT synergistically composited electrospun thermoplastic polyurethane yarns for wearable sensing. *J. Mater. Chem. C* 2018, 6 (9), 2258–2269.
- (34) Guan, X.; Zheng, G.; Dai, K.; Liu, C.; Yan, X.; Shen, C.; Guo, Z. Carbon nanotubes-adsorbed electrospun PA66 nanofiber bundles with improved conductivity and robust flexibility. *ACS Appl. Mater. Interfaces* **2016**, 8 (22), 14150–14159.
- (35) Zhao, M.; Meng, L.; Ma, L.; Ma, L.; Yang, X.; Huang, Y.; Ryu, J. E.; Shankar, A.; Li, T.; Yan, C.; Guo, Z. Layer-by-Layer grafting CNTs onto carbon fibers surface for enhancing the interfacial properties of epoxy resin composites. Compos. *Compos. Sci. Technol.* **2018**, *154*, 28–36.
- (36) Sun, K.; Xie, P.; Wang, Z.; Su, T.; Shao, Q.; Ryu, J. E.; Zhang, X.; Guo, J.; Shankar, A.; Li, J. Flexible polydimethylsiloxane/multi-walled carbon nanotubes membranous metacomposites with negative permittivity. *Polymer* **2017**, *125*, 50–57.
- (37) Wu, Z.; Gao, S.; Chen, L.; Jiang, D.; Shao, Q.; Zhang, B.; Zhai, Z.; Wang, C.; Zhao, M.; Ma, Y.; Zhang, X.; Weng, L.; Zhang, M.; Guo, Z. Electrically insulated epoxy nanocomposites reinforced with synergistic core—shell SiO₂@MWCNTs and montmorillonite bifillers. *Macromol. Chem. Phys.* **2017**, 218 (23), 1700357-1–1700357-9.
- (38) Zhang, K.; Li, G. H.; Feng, L. M.; Wang, N.; Guo, J.; Sun, K.; Yu, K. X.; Zeng, J. B.; Li, T.; Guo, Z.; Wang, M. Ultralow percolation threshold and enhanced electromagnetic interference shielding in poly(l-lactide)/multi-walled carbon nanotube nanocomposites with electrically conductive segregated networks. *J. Mater. Chem. C* **2017**, *5*, 9359–9369.
- (39) Zhang, Q.; Huang, J. Q.; Qian, W. Z.; Zhang, Y. Y.; Wei, F. The road for nanomaterials industry: a review of carbon nanotube production, post-treatment, and bulk applications for composites and energy storage. *Small* **2013**, *9* (8), 1237–1265.
- (40) Zhu, L.; Zhu, W.; Cheng, X. B.; Huang, J. Q.; Peng, H.; Yang, S. H.; Zhang, Q. Cathode materials based on carbon nanotubes for high-energy-density lithium—sulfur batteries. *Carbon* **2014**, *75*, 161–168.
- (41) Huang, Z. P.; Xu, J. W.; Ren, Z. F.; Wang, J. H.; Siegal, M. P.; Provencio, P. N. Growth of highly oriented carbon nanotubes by plasma-enhanced hot filament chemical vapor deposition. *Appl. Phys. Lett.* **1998**, 73 (26), 3845–3847.

- (42) Thess, A.; Lee, R.; Nikolaev, P.; Dai, H.; Petit, P.; Xu, C.; Lee, Y. H.; Kim, S. G.; Rinzler, A. G.; Colbert, D. T.; Scuseria, G. E.; Tománek, D.; Fischer, J. E.; Smalley, R. E. Crystalline ropes of metallic carbon nanotubes. *Science* 1996, 273 (5274), 483–487.
- (43) Wang, Y.; Kim, M. J.; Shan, H.; Kittrell, C.; Fan, H.; Ericson, L. M.; Hwang, W. F.; Arepalli, S.; Hauge, R. H.; Smalley, R. E. Continued growth of single-walled carbon nanotubes. *Nano Lett.* **2005**, *5* (6), 997–1002.
- (44) Kumar, M.; Ando, Y. Chemical vapor deposition of carbon nanotubes: A review on growth mechanism and mass production. *J. Nanosci. Nanotechnol.* **2010**, *10* (6), 3739–3758.
- (45) Gao, Z.; Zhang, Y.; Song, N.; Li, X. Biomass-derived renewable carbon materials for electrochemical energy storage. *Mater. Res. Lett.* **2017**, *5* (2), 69–88.
- (46) Xu, J.; Zhou, K.; Chen, F.; Chen, W.; Wei, X.; Liu, X.-W.; Liu, J. Natural integrated carbon architecture for rechargeable lithium—sulfur batteries. ACS Sustainable Chem. Eng. 2016, 4 (3), 666–670.
- (47) Gu, X.; Wang, Y.; Lai, C.; Qiu, J.; Li, S.; Hou, Y.; Martens, W.; Mahmood, N.; Zhang, S. Microporous bamboo biochar for lithium-sulfur batteries. *Nano Res.* **2015**, 8 (1), 129–139.
- (48) Guo, J.; Zhang, J.; Jiang, F.; Zhao, S.; Su, Q.; Du, G. Microporous carbon nanosheets derived from corncobs for lithium—sulfur batteries. *Electrochim. Acta* **2015**, *176*, 853–860.
- (49) Gong, K.; Hu, Q.; Yao, L.; Li, M.; Sun, D.; Shao, Q.; Qiu, B.; Guo, Z. Ultrasonic pretreated sludge derived stable magnetic active carbon for Cr (VI) removal from wastewater ultrasonic pretreated sludge derived stable magnetic active carbon for Cr (VI) removal from wastewater. ACS Sustainable Chem. Eng. 2018, 6 (6), 7283–7291.
- (50) Wang, X.; Zeng, X.; Cao, D. Biomass-derived nitrogen-doped porous carbons (NPC) and NPC/polyaniline compositesas high performance supercapacitor materials. *Eng. Sci.* **2018**, *1*, 55–63.
- (51) Lu, S.; Chen, Y.; Zhou, J.; Wang, Z.; Wu, X.; Gu, J.; Zhang, X.; Pang, A.; Jiao, Z.; Jiang, L. A sheet-like carbon matrix hosted sulfur as cathode for high-performance lithium-sulfur batteries. *Sci. Rep.* **2016**, *6*, 20445.
- (52) Chen, F.; Yang, J.; Bai, T.; Long, B.; Zhou, X. Biomass wastederived honeycomb-like nitrogen and oxygen dual-doped porous carbon for high performance lithium-sulfur batteries. *Electrochim. Acta* **2016**, *192*, 99–109.
- (53) Gao, Z.; Bumgardner, C.; Song, N.; Zhang, Y.; Li, J.; Li, X. Cotton-textile-enabled flexible self-sustaining power packs via roll-to-roll fabrication. *Nat. Commun.* **2016**, *7*, 11586.
- (54) Gao, Z.; Song, N.; Zhang, Y.; Li, X. Cotton-textile-enabled, flexible lithium-ion batteries with enhanced capacity and extended lifespan. *Nano Lett.* **2015**, *15* (12), 8194–8203.
- (55) Gao, Z.; Schwab, Y.; Zhang, Y.; Song, N.; Li, X. Ferromagnetic nanoparticle-assisted polysulfide trapping for enhanced lithium-sulfur batteries. *Adv. Funct. Mater.* **2018**, 28, 1800563-1–1800563-9.
- (56) Zhang, Y.; Gao, Z.; Song, N.; Li, X. High-performance supercapacitors and batteries derived from activated banana-peel with porous structures. *Electrochim. Acta* **2016**, 222, 1257–1266.
- (57) Zhang, Y.; Gao, Z.; Li, X. Capillarity composited recycled paper/graphene scaffold for lithium-sulfur batteries with enhanced capacity and extended lifespan. *Small* **2017**, *13*, 1701927.
- (58) Goesaert, H.; Brijs, K.; Veraverbeke, W. S.; Courtin, C. M.; Gebruers, K.; Delcour, J. A. Wheat flour constituents: how they impact bread quality, and how to impact their functionality. *Trends Food Sci. Technol.* **2005**, *16*, 12–30.
- (59) Švec, I.; Hrušková, M. Wheat flour fermentation study. *Czech J. Food Sci.* **2011**, 22 (1), 17–23.
- (60) Balasubramanian, M. K.; Bi, E.; Glotzer, M. Comparative analysis of cytokinesis in budding yeast, fission yeast and animal cells. *Curr. Biol.* **2004**, *14* (18), 806–818.
- (61) Wang, X.; Niu, Z.; Li, S.; Wang, Q.; Li, X. Nanomechanical characterization of polyaniline coated tobacco mosaic virus nanotubes. *J. Biomed. Mater. Res., Part A* **2008**, 87 (1), 8–14.

- (62) De Pablo, P. J.; Schaap, I. A. T.; MacKintosh, F. C.; Schmidt, C. F. Deformation and collapse of microtubules on the nanometer scale. *Phys. Rev. Lett.* **2003**, *91* (9), 98101.
- (63) Qi, X.; Xu, J.; Hu, Q.; Deng, Y.; Xie, R.; Jiang, Y.; Zhong, W.; Du, Y. Metal-free carbon nanotubes: synthesis, and enhanced intrinsic microwave absorption properties. *Sci. Rep.* **2016**, *6*, 1–11.
- (64) Sandhu, H. P. S.; Manthey, F. A.; Simsek, S. Ozone gas affects physical and chemical properties of wheat (triticum aestivum l.) starch. *Carbohydr. Polym.* **2012**, 87 (2), 1261–1268.
- (65) Stamatin, I.; Morozan, A.; Dumitru, A.; Ciupina, V.; Prodan, G.; Niewolski, J.; Figiel, H. The synthesis of multi-walled carbon nanotubes (MWNTs) by catalytic pyrolysis of the phenol-formaldehyde resins. *Phys. E* **2007**, *37*, 44–48.
- (66) Li, G.; Sun, J.; Hou, W.; Jiang, S.; Huang, Y.; Geng, J. Three-dimensional porous carbon composites containing high sulfur nanoparticle content for high-performance lithium-sulfur batteries. *Nat. Commun.* **2016**, *7*, 10601-1–10601-10.
- (67) Zeng, Q.; Wang, D.-W.; Wu, K.-H.; Li, Y.; Condi de Godoi, F.; Gentle, I. R. Synergy of nanoconfinement and surface oxygen in recrystallization of sulfur melt in carbon nanocapsules and the related Li–S cathode properties. *J. Mater. Chem. A* **2014**, 2 (18), 6439–6447.
- (68) Ferrari, A.; Robertson, J. Interpretation of raman spectra of disordered and amorphous carbon. *Phys. Rev. B: Condens. Matter Mater. Phys.* **2000**, *61* (20), 14095–14107.
- (69) Malard, L. M.; Pimenta, M. A.; Dresselhaus, G.; Dresselhaus, M. S. Raman spectroscopy in graphene. *Phys. Rep.* **2009**, 473 (5–6), 51–87.
- (70) Dzsaber, S.; Negyedi, M.; Bernath, B.; Gyure, B.; Feher, T.; Kramberger, C.; Pichler, T.; Simon, F. A fourier transform raman spectrometer with visible laser excitation. *J. Raman Spectrosc.* **2015**, 46 (3), 327–332.
- (71) Nazar, L. F.; Cuisinier, M.; Pang, Q. Lithium-sulfur batteries. *MRS Bull.* **2014**, 39 (5), 436–442.
- (72) Yuan, L.; Qiu, X.; Chen, L.; Zhu, W. New insight into the discharge process of sulfur cathode by electrochemical impedance spectroscopy. *J. Power Sources* **2009**, *189* (1), 127–132.
- (73) Cabana, J.; Monconduit, L.; Larcher, D.; Palacín, M. R. Beyond intercalation-based Li-ion batteries: the state of the art and challenges of electrode materials reacting through conversion reactions. *Adv. Mater.* **2010**, *22* (35), 170–192.
- (74) Zhang, B.; Qin, X.; Li, G. R.; Gao, X. P. Enhancement of long stability of sulfur cathode by encapsulating sulfur into micropores of carbon spheres. *Energy Environ. Sci.* **2010**, 3 (10), 1531.
- (75) Xin, S.; Gu, L.; Zhao, N.-H.; Yin, Y.-X.; Zhou, L.-J.; Guo, Y.-G.; Wan, L.-J. Smaller sulfur molecules promise better lithium-sulfur batteries. *J. Am. Chem. Soc.* **2012**, *134* (45), 18510–18513.
- (76) Wang, J.; Yang, J.; Wan, C.; Du, K.; Xie, J.; Xu, N. Sulfur composite cathode materials for rechargeable lithium batteries. *Adv. Funct. Mater.* **2003**, *13* (6), 487–492.
- (77) Cheng, F.; Wang, H.; Zhu, Z.; Wang, Y.; Zhang, T.; Tao, Z.; Chen, J. Porous $LiMn_2O_4$ nanorods with durable high-rate capability for rechargeable li-ion batteries. *Energy Environ. Sci.* **2011**, 4 (9), 3668–3675.
- (78) Romanos, J.; Beckner, M.; Rash, T.; Firlej, L.; Kuchta, B.; Yu, P.; Suppes, G.; Wexler, C.; Pfeifer, P. Nanospace engineering of KOH activated carbon. *Nanotechnology* **2012**, 23 (1), 015401.
- (79) Homma, Y.; Kobayashi, Y.; Ogino, T.; Takagi, D.; Ito, R.; Jung, Y. J. Y. Y. J.; Ajayan, P. M. P. Role of transition metal catalysts in single-walled carbon nanotube growth in chemical vapor deposition. *J. Phys. Chem. B* **2003**, *107* (44), 12161–12164.
- (80) Wang, D. W.; Zeng, Q.; Zhou, G.; Yin, L.; Li, F.; Cheng, H. M.; Gentle, I. R.; Lu, G. Q. M. Carbon–sulfur composites for Li–S batteries: status and prospects. *J. Mater. Chem. A* **2013**, *1* (33), 9382–9394.
- (81) Zhang, J.; Shi, Y.; Ding, Y.; Peng, L.; Zhang, W.; Yu, G. A conductive molecular framework derived Li2S/N,P-codoped carbon cathode for advanced lithium–sulfur batteries. *Adv. Energy Mater.* **2017**, 7 (14), 1602876-1–1602876-7.